Journal of Physics:
Condensed Matter

PAPER • **OPEN ACCESS**

Local dielectric function of hBN-encapsulated WS_2 flakes grown by chemical vapor deposition

To cite this article: Marzia Ferrera *et al* 2023 *J. Phys.: Condens. Matter* **35** 274001

OPEN ACCESS
IOP Publishing
Journal of Physics: Condensed Matter
J. Phys.: Condens. Matter **35** (2023) 274001 (8pp)
https://doi.org/10.1088/1361-648X/acc918

Local dielectric function of hBN-encapsulated WS_2 flakes grown by chemical vapor deposition

Marzia Ferrera[1,2,*], Apoorva Sharma[3], Ilya Milekhin[3,4], Yang Pan[3,4], Domenica Convertino[5], Simona Pace[5,6], Giorgio Orlandini[5], Ermes Peci[1], Lorenzo Ramò[1], Michele Magnozzi[1,7], Camilla Coletti[5,6], Georgeta Salvan[3], Dietrich R T Zahn[3,4], Maurizio Canepa[1] and Francesco Bisio[8]

[1] OptMatLab, Physics Department, Università di Genova, via Dodecaneso 33, 16146 Genova, Italy
[2] Istituto Italiano di Tecnologia, via Morego 30, 16163 Genova, Italy
[3] Semiconductor Physics, Chemnitz University of Technology, D-09107 Chemnitz, Germany
[4] Center for Materials, Architectures and Integration of Nanomembranes (MAIN), Chemnitz University of Technology, D-09107 Chemnitz, Germany
[5] Center for Nanotechnology Innovation IIT@NEST, Piazza San Silvestro 12, 56127 Pisa, Italy
[6] Graphene Labs, Istituto Italiano di Tecnologia, via Morego 30, 16163 Genova, Italy
[7] INFN, Sezione di Genova, via Dodecaneso 33, 16146 Genova, Italy
[8] CNR-SPIN, corso Perrone 24, 16152 Genova, Italy

E-mail: marzia.ferrera@iit.it

Received 30 November 2022, revised 27 March 2023
Accepted for publication 30 March 2023
Published 12 April 2023

Abstract

Hexagonal boron nitride (hBN), sometimes referred to as white graphene, receives growing interest in the scientific community, especially when combined into van der Waals (vdW) homo- and heterostacks, in which novel and interesting phenomena may arise. hBN is also commonly used in combination with two-dimensional (2D) semiconducting transition metal dichalcogenides (TMDCs). The realization of hBN-encapsulated TMDC homo- and heterostacks can indeed offer opportunities to investigate and compare TMDC excitonic properties in various stacking configurations. In this work, we investigate the optical response at the micrometric scale of mono- and homo-bilayer WS_2 grown by chemical vapor deposition and encapsulated between two single layers of hBN. Imaging spectroscopic ellipsometry is exploited to extract the local dielectric functions across one single WS_2 flake and detect the evolution of excitonic spectral features from monolayer to bilayer regions. Exciton energies undergo a redshift by passing from hBN-encapsulated single layer to homo-bilayer WS_2, as also confirmed by photoluminescence spectra. Our results can provide a reference for the study of the dielectric properties of more complex systems where hBN is combined with other 2D vdW materials into heterostructures and are stimulating towards the investigation of the optical response of other technologically-relevant heterostacks.

* Author to whom any correspondence should be addressed.

Supplementary material for this article is available online

Keywords: van der Waals heterostructures, hexagonal boron nitride, transition metal dichalcogenides, excitons, imaging ellipsometry

(Some figures may appear in colour only in the online journal)

1. Introduction

The family of van der Waals (vdW) materials offers a wide range of two-dimensional (2D) atomic crystals with diverse electronic properties [1, 2]. Regarding optoelectronics and photonics applications, group VI semiconducting transition metal dichalcogenides (TMDCs) show great potential due to their indirect-to-direct bandgap crossover at the single-layer limit, with optical bandgap values falling in the visible and near-infrared energy range [3–6]. The optical properties of mono- and few-layer TMDCs are dictated by tightly bound excitons [7–13], Coulomb-correlated electron–hole pairs. The quantum confinement of the exciton wavefunction and the reduced dielectric screening from the environment result in excitonic binding energies of the order of 500 meV [14, 15], which is one to two orders of magnitude larger than conventional quantum-well structures used for optoelectronic devices.

However, the three-atom-thick semiconducting TMDCs absorb approximately only 10% of incident photons in correspondence with the bandgap excitonic resonance [4]. This is, in absolute terms, too low to satisfy the requirements for the realization of efficient devices. An effective strategy to engineer light–matter interaction in 2D TMDCs, while preserving the benefits arising from their reduced dimensionality, is their integration with other materials in metamaterials or superlattices [16–19]. By exploiting sequential layer-by-layer assembly, homo- and heterostacks of 2D atomic crystals can be obtained, opening new opportunities for the design and realization of high quality, and, possibly, wafer-scale devices with singular properties [2, 17, 20, 21]. Accordingly, several stacking configurations with various functionalities were recently addressed, such as homo-bilayer TMDCs with different stacking order, i.e. 2H or 3R, to explore interlayer excitons [22–24], MoS_2/WS_2 heterostructures to investigate ultrafast charge transfer [25], various TMDC twisted heterostructures with lateral superlattices with the emergence of Moiré excitons [26–28]. In addition, nanohybrid systems involving 2D TMDCs, such as MoS_2/TiO_2 [29] or In_2S_3/MoS_2 [30], proved efficient for photocatalytic applications showing an increased photodegradation capability over the pure photocatalysts (e.g. TiO_2 or In_2S_3) [29–31].

When dealing with such kind of systems, it is crucial to consider how the excitonic response of 2D TMDCs, acting as building blocks of the vertical stack, are modified by the presence of adjacent layers, in comparison to the freestanding case. As an example, the encapsulation of TMDCs in hexagonal boron nitride (hBN) provides surface protection from contaminants, atomic flatness of the substrate surface, and prevents doping from the substrate underneath [32–34]. Vertical stacks, in which hBN was integrated with TMDCs materials have been extensively investigated in the literature. Cadiz *et al* [33] showed that the encapsulation of monolayer (ML) TMDCs in hBN can suppress the inhomogeneous contribution to the exciton linewidth [35]. Interlayer excitons were observed in hBN-encapsulated 2H homobilayer MoS_2 by means of reflectivity measurements in the temperature range $T = 4$–300 K [22]. The improvement of the optical quality of TMDC flakes grown by chemical vapor deposition (CVD) via hBN-encapsulation made also possible to study the effect of stacking (2H or 3R) on the excitonic properties of homobilayer MoS_2 [23]. More in general, in the last years, hBN-encapsulation of 2D materials was adopted as an effective tool to obtain high quality samples and devices with the desired properties. TMDCs sandwiched between hBN layers were fabricated to shed light on their ultrafast exciton dynamics [36], they were integrated as functional parts of nanophotonic architectures [37], and they were directly patterned via top-down lithography for nanoscale optoelectronics [38]. These examples just give the taste of the growing interest in such kind of systems of the scientific community. The hBN has not only the role of encapsulating material. Recently, parallel-stacked bilayer hBN was used as a testbed to demonstrate the concept of interfacial ferroelectricity [39–42]; in another work, hBN was integrated with TMDCs to realize a large area vdW superlattice stacked on a gold back reflector supporting strongly coupled exciton-polaritons at room temperature [19]. In general, when dealing with the design of optical metamaterials from atomically thin layers, thorough knowledge of the optical properties of the constituent layers in the heterostack is pivotal for the optimization of such kind of systems.

Recent works showed that the combination of optical techniques with a micrometric lateral resolution, such as imaging spectroscopic ellipsometry (ISE) and photoluminescence (PL) spectroscopy, is effective to study the light absorption and emission-related properties of ML-TMDCs by probing, respectively, their dielectric function and the PL [43–49].

By following a similar approach, here we exploit ISE and PL to investigate with a spatial resolution at the micrometric scale the optical properties of WS_2 flakes grown by CVD and sandwiched between two single layers of hBN. The local dielectric functions of the building blocks of a three-layer (hBN/ML-WS_2/hBN) and a four-layer stack (hBN/BL-WS_2/hBN) were extracted. Additionally, the PL spectroscopy characterization coupled with the ISE results provided a complete picture of the optical response of the heterostructures, since they allowed also tiny variations in the excitonic features to be detected by passing from ML to BL-WS_2, or by varying

the dielectric environment surrounding the semiconducting WS_2 (presence or absence of hBN encapsulating layers). The method presented here is general and applicable to a wide range of systems, where hBN is combined with other 2D atomic crystals to form even more complex structures than the one investigated here. The possibility to easily access to the optical properties of vdW heterostacks is a prerequisite in view of their exploitation for technologically relevant applications.

2. Experimental section

2.1. Materials

In the present study, the local properties of WS_2 flakes encapsulated by hBN were analyzed. The flakes were grown on Si/SiO_2 substrate via liquid precursor chemical vapor deposition (LqP-CVD) in a two-zone horizontal furnace (Lenton) [43, 44, 50–52]. The growth mechanism of the LqP-CVD process was reported in detail in [50], and here the main steps are summarized. An aqueous solution containing a tungsten precursor (ammonium metatungstate hydrate, AMT, Sigma-Aldrich, 463922, 0.2 g in 20 ml of deionized (DI) water) was mixed with an aqueous solution with the growth promoter (NaOH, Sigma-Aldrich, S8045, 0.2 g in 20 ml of DI water). A small amount of a density gradient (iodixanol, OPTI, OptiPrep™, Sigma-Aldrich, D1556) was also added to the aqueous solution to increase the viscosity and improve the adhesion of the solution to the substrate. The obtained solution was spin-coated on the SiO_2/Si substrate, which was previously sonicated in acetone and isopropanol and treated with an oxygen plasma. The spin-coated substrate was placed in the high temperature region of the reactor and heated in atmospheric pressure at 800 °C over a time interval of 6 min under constant Ar/H_2 (H_2 3%) flux, while sulfur pellets were maintained at 180 °C–210 °C to induce their sublimation. After the growth, a constant Ar flux naturally cooled down the reactor. In the ramp-up, above 550 °C the AMT is thermally decomposed in the W precursor WO_3. Sodium hydroxide is used as promoter to facilitate the adhesion of the precursor on the SiO_2 substrate by forming clusters of intermediate compounds (Na_2WO_4), thus increasing the wettability of W to improve the lateral growth of the WS_2 flakes by acting as an additional source of W. Following S sublimation, WS_2 flakes are grown from the S vapor reaction with both the WO_3 precursor and the previously formed intermediated compounds. The relative ratio of Na/W in the aqueous solution was varied to find the best growth uniformity and flake dimension. By optimizing the mixed solution (ratio 1.5:2:1:2 (AMT:NaOH:OPTI:DI)), the heating temperature and the dwelling time, large-scale triangular monolayer WS_2 flakes were successfully grown. 2H and 3R stacked bilayer WS_2 crystals were also randomly distributed inside the sample. Unlike crystalline bulk and 2D substrates, such as α-Al_2O_3 (0001) and graphene, which allow for the epitaxial growth of WS_2 via low-pressure CVD and metal-organic CVD [53–55], the non-crystalline nature of the SiO_2 substrate did not allow an epitaxial orientation of the flakes to be obtained.

For the heterostructure preparation, a semidry transfer approach was used [34, 56–58]. The sample extracted from the CVD reactor was covered by a double-layer polymeric membrane of polymethylmethacrylate (PMMA AR-P 679.02, Allresist) and 15% polypropylene carbonate in anisole (PPC, Sigma-Aldrich), which were sequentially spun and baked at 90 °C for 2 min.

The sample was then covered with a few-millimeter-thick polydimethylsiloxane frame, and immersed in NaOH 1 M solution at 70 °C, until the membrane was completely detached. By using a transfer setup, the WS_2 flakes were deterministically transferred from the growth substrate to a $hBN/SiO_2/Si$ target sample. The hBN was previously transferred on the 300 nm SiO_2/Si substrate via electrochemical delamination of commercially available hBN from a copper substrate (Graphene Supermarket). The CVD-grown hBN had a nominal monolayer thickness [34, 59, 60] and was directly used as received. To complete the heterostack, another layer of hBN was vertically stacked on top of the heterostructure, by repeating the same transfer procedure. At the end of each transfer, the polymeric membrane was removed in acetone and isopropanol.

2.2. Methods

2.2.1. ISE. The optical properties of the vdW heterostructures at the microscale were investigated by using a nanofilm_ep4 from Accurion GmbH. In ellipsometry, the variation of light polarization upon reflection from the sample is quantified by two angles, Ψ and Δ, defined as:

$$\tan\Psi\, e^{i\Delta} = \frac{|r_p|}{|r_s|} e^{i(\delta_p - \delta_s)}$$

in which $|r_{s,p}|$ and $\delta_{s,p}$ are the amplitudes and phases of the Fresnel coefficients $r_{s,p}$, respectively [61]. The ellipsometry data were acquired in the nulling mode. The measurements were performed with a 20× objective. The spectra were collected from different regions of interest (ROIs) in the 400–800 nm wavelength range (1.5–3.1 eV energy range), with a step of 5 nm. The angle of incidence spanned from 45° to 70°, with a step of 5°.

2.2.2. Raman and PL spectroscopies. For Raman and PL measurements a LabRam HR800 (Horiba Jobin Yvon GmbH, Bensheim, Germany) with an optical microscope Olympus BX40 (Olympus Corporation, Hamburg, Germany) was used. An incident laser beam with a wavelength of 514.7 nm and a power of 100 μW was directed onto the sample through a 100× objective (numerical aperture NA = 0.9). The laser spot size was approximately 1 μm in diameter. Light was collected in the back-scattering geometry. The PL and Raman signals were detected by a liquid-nitrogen-cooled back-illuminated

charge-coupled device. The spectral resolution was 2.5 cm^{-1} for Raman and 1.2 meV for PL, respectively.

3. Results and discussion

The investigated system is shown in the optical micrograph of figure 1(a). The CVD-grown WS_2 flake is characterized by a typical triangular shape and a monolayer thickness extending for hundreds of microns across [43, 44, 52]. At the center of the flake, a bilayer region with a 0° twist angle is present (3R stacking). 3R together with 2H (60° twist angle) stackings correspond to the most stable configurations of TMDC homobilayers, and can naturally occur during the CVD growth of the flakes [23, 62]. The hBN regions can be visualized in the optical image as bluish areas, thanks to the optical contrast provided by the 300 nm-thick SiO_2/Si substrate [63]. Some impurities, which typically occur at the edge of the hBN film [59], can facilitate the recognition of the area, where both the top and bottom layers of hBN are present (white dotted line in figure 1(a)).

A scheme of the heterostructures is shown in figure 1(b). Both three-layer (hBN/ML-WS_2/hBN) and four-layer (hBN/BL-WS_2/hBN) vertical stacks were considered.

Further confirmation of the thickness of different regions of the WS_2 flake was provided by Raman and PL spectroscopy. In figure 1(c) representative Raman spectra acquired with 514.7 nm laser excitation are shown. The main WS_2 Raman peaks can be recognized: the first order modes at the Brillouin zone center, $E^1_{2g}(\Gamma)$ and $A_{1g}(\Gamma)$, and the second-order longitudinal acoustic mode at the M point, 2LA(M). From the fitting of the Raman spectra (see figure S1(a) in the supplementary data), the Raman shift of the main modes was extracted. For ML-WS_2, the 2LA(M) the $E^1_{2g}(\Gamma)$ and $A_{1g}(\Gamma)$ modes fall at 352.5 ± 0.2 cm^{-1} and 356.9 ± 0.2 cm^{-1} and 418.9 ± 0.2 cm^{-1}, respectively. By passing from monolayer (red line) to bilayer (blue line) regions a hardening (blueshift) of $A_{1g}(\Gamma)$ mode occurs, from approximately 419 cm^{-1}–420 cm^{-1}, in agreement with the literature [64, 65]. The E^1_{2g}/A_{1g} Raman mode intensity ratio is approximately 2 for ML-WS_2, while it approaches unity for the BL region, in line with previous results [53, 66, 67]. In addition, a stiffening of the A_{1g} mode can be observed when a hBN layer is intercalated between the WS_2 flake and the substrate (see figure S1(b) in the supplementary data, where Raman spectra of ML-WS_2/SiO_2/Si and hBN/WS_2/hBN/SiO_2/Si are reported). The presence of the hBN layer between the SiO_2 and the WS_2 can indeed reduce the level of electron doping from SiO_2 substrate, thus affecting the A_{1g} mode frequency [68–70]. The strong PL signal from ML-WS_2 peaking at 2.0 eV (red line) in figure 1(d) and the very weak redshifted PL signal coming from the BL-WS_2 (blue line) is a fingerprint of the direct-to-indirect band gap transition, which takes place in the single layer limit. Both the Raman and PL properties were homogeneous across the inner triangular regions of the ML-WS_2 flake [43], as shown by the PL map and the Raman spectra acquired from different

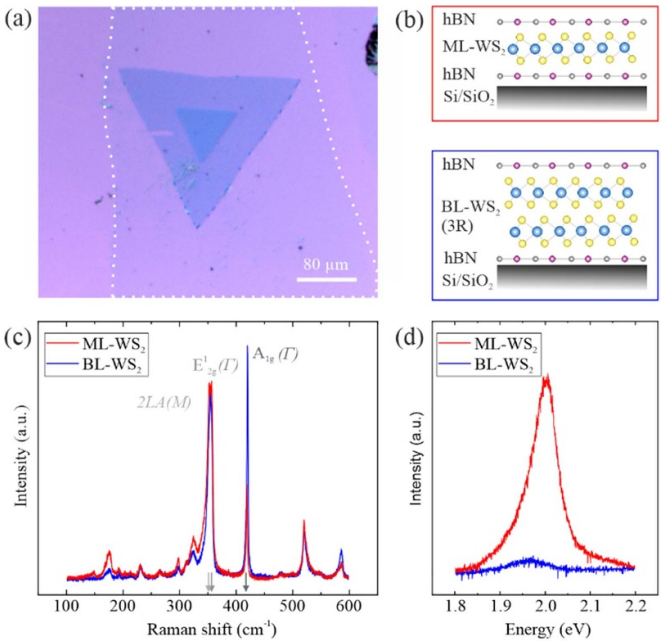

Figure 1. (a) Optical micrograph of a hBN-encapsulated WS_2 flake grown by CVD. At the center of the flake, a bilayer region (3R stacking) is present; the remaining area is a monolayer. The dotted white line delimits the area, where the top and bottom hBN layers are present. (b) Schemes of the investigated vdW heterostructures, hBN/ML-WS_2/hBN and hBN/3R BL-WS_2/hBN on SiO_2/Si substrate. (c) Raman spectra of hBN-encapsulated ML-WS_2 (red) and BL-WS_2 (blue). The main WS_2 Raman modes are labeled. The corresponding frequencies are indicated by the gray arrows. (d) PL spectra of hBN-encapsulated ML-WS_2 (red) and BL-WS_2 (blue).

spots across the hBN-encapsulated WS_2 flake (figures S2(a) and (b) in the supplementary data).

The layer dielectric functions within the vdW heterostack were investigated by means of ISE. Angle-dependent (Ψ, Δ) spectra were collected with a micrometric spatial resolution for the hBN/ML-WS_2/hBN/SiO_2/Si (red curves of figure 2(a)) and hBN/BL-WS_2/hBN/SiO_2/Si (blue curves of figure 2(b)). Each set of (Ψ,Δ) spectra in the graphs is composed of (Ψ,Δ) values averaged across the corresponding ROI. In the left part of figure 2, each ROI is delimited by a white dashed line. Angle-dependent (Ψ,Δ) spectra were also acquired for the hBN/SiO_2/Si system, as shown in figure S3(a) in the supplementary data.

To interpret the ellipsometric data, we set up an optical model of each heterostack using a multi-step approach. The model consists of a series of optical layers, each characterized by its own thickness and complex dielectric function. The interfaces between the layers were assumed to be sharp and planar, and characterized by Fresnel boundary conditions. We started by modeling the simplest system, i.e. hBN/SiO_2/Si and gradually increased the model complexity up to hBN/ML-WS_2/hBN/SiO_2/Si and, then, hBN/BL-WS_2/hBN/SiO_2/Si. Finally, the dielectric functions of ML- and BL-WS_2 in the heterostructures were extracted by means of a best-fit procedure.

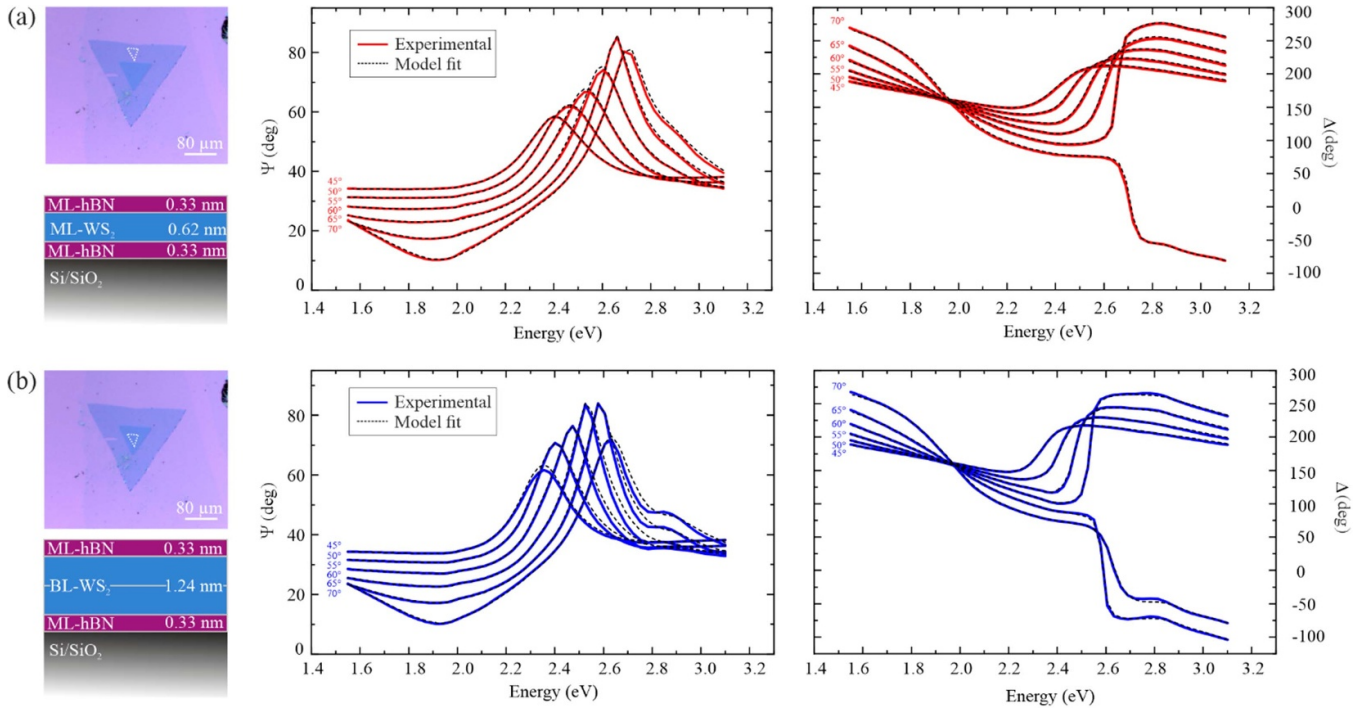

Figure 2. Angle-dependent experimental (Ψ, Δ) spectra acquired for (a) hBN/ML-WS_2/hBN/SiO_2/Si (red curves) and (b) hBN/BL-WS_2 /hBN/SiO_2/Si (blue curves) heterostructures. The data were collected from the ROIs delimited by the dashed white lines in the optical images on the left side. The scheme of the optical model used for each layered stack is also shown on the left side. The dashed black lines in the graphs correspond to the best fitting curves.

First, micro-SE data acquired on the hBN/SiO_2/Si system were independently modeled, in order to have an independent assessment of the hBN thickness. To this end, the dielectric functions of SiO_2 and Si were taken from the WVASE software libraries [71] and a thickness of 288.43 $\pm$ 0.03 nm was extracted for the SiO_2 film on top of Si. For the hBN layer, we employed the hBN optical constants reported in a recent work [72], similar to other recently reported literature values [73–75]. We obtained a hBN thickness of 0.65 $\pm$ 0.01 nm, in good agreement with the expectations for a two-layers hBN system (figure S3(a) in the supplementary data), where each layer has a nominal thickness of less than 0.420 nm [59] (see section 2.1 for more details).

The information obtained from this fit was fed in the optical model of the hBN/ML-WS_2/hBN/SiO_2/Si system. Here, the thickness of ML-WS_2 was set to 0.62 nm [44, 76] and the ML-WS_2 optical properties were modeled by superimposing Herzinger-Johs PSEMI and Tauc-Lorentz oscillators [77–79], as reported in the literature for other ML-TMDC systems [43, 44, 49, 80]. In the fit, given the large number of potentially free parameters, we only allowed the amplitudes and energies of the oscillators of the WS_2 layer to be varied. We point out that few-layer vdW materials are naturally characterized by strongly anisotropic optical properties [81]. Indeed, in the out-of-plane direction there is a complete lack of translational symmetry, hence no electronic band structure can be defined. From the experimental point of view, however, in presence of mono- and few-layer-thick flakes, the sensitivity of angle-resolved spectroscopic ellipsometry to the out-of-plane component of the dielectric tensor almost drops to zero. As a consequence, atomically thick TMDCs are usually treated as optically-isotropic systems, even though this is not, in principle, a correct physical representation. The extracted dielectric function represents, with very good approximation, their in-plane optical properties.

The model employed for the ML-WS_2-based heterostructure was then adapted for the hBN/BL-WS_2/hBN/SiO_2/Si stack. Also here, only the amplitudes and energies of the oscillators of the WS_2 film were left free to vary in the fit, while all the other parameters were kept fixed. The best fitting curves are shown in the graphs of figures 2(a) and (b) as the black dashed lines overlapped to the experimental data.

From the analysis of micro-SE data, the local dielectric functions (ε: $= \varepsilon_1 + i\varepsilon_2$, with ε_1 (ε_2) real (imaginary) part) of ML- and BL-WS_2 sandwiched between hBN layers were extracted, as shown, respectively, by the red and blue curves of figure 3. The dielectric function of a ML-WS_2 flake directly transferred onto SiO_2/Si substrate (with no hBN encapsulation) was also obtained from ISE data (see figure S3(b) in the supplementary data), and is shown here as a reference (dashed black line). In general, the complex dielectric function of WS_2 in the investigated spectral range exhibits resonances ascribed to the presence of the so-called A, B, and C excitons [15, 82]. In correspondence to each excitonic transition, a wiggle (peak) appears in the real (imaginary) part of the dielectric function. For ML-WS_2 (red line), the extracted

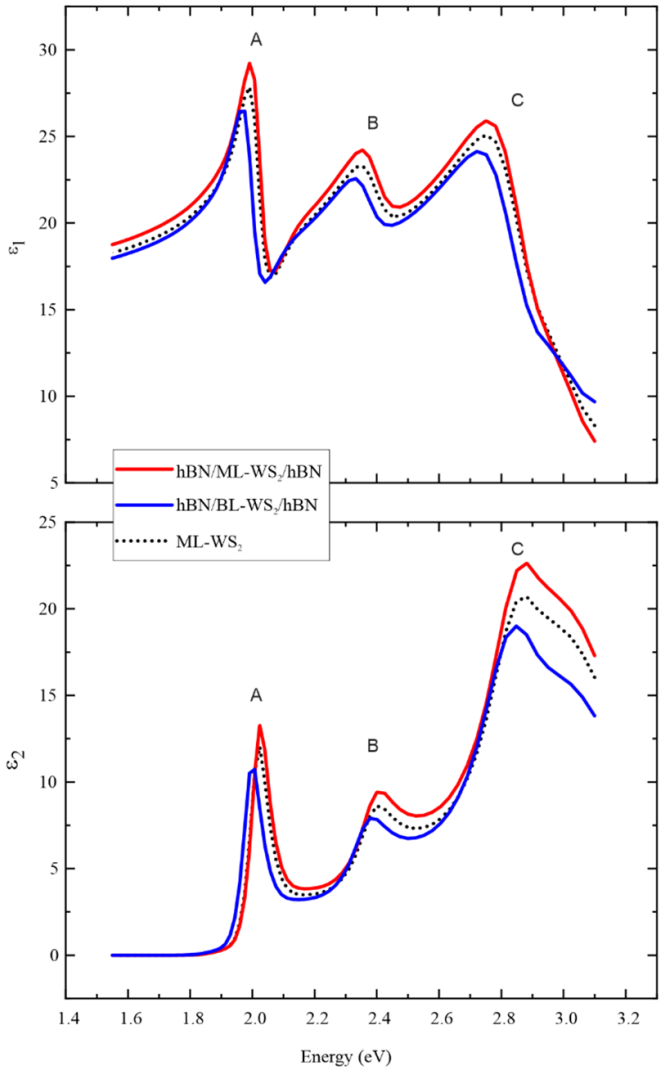

Figure 3. Real (top, ε_1) and imaginary (bottom, ε_2) parts of the dielectric function of hBN-encapsulated ML-WS_2 (red curves) and 3R BL-WS_2 (blue curves). For comparison, the dielectric function of ML-WS_2 on SiO_2/Si substrate without hBN encapsulation is shown (dotted black curve).

exciton energies are 2.022 ± 0.003 eV, 2.397 ± 0.003 eV, and 2.785 ± 0.003 eV. In ML-TMDCs, A excitons are the lowest-energy bright-valley excitons, and, together with B excitons, are related to the optical interband transitions at the K point of the Brillouin zone [83]. The energy separation between A and B excitonic features of approximately 375 meV can be used to experimentally determine the value of the spin-splitting in the valence band. The strong absorption due to the C excitonic feature can be ascribed to the phenomenon of band nesting between the Γ and K symmetry points in the Brillouin zone.

The dielectric function of BL-WS_2 is analogous to the single-layer, with some variations occurring in correspondence to the resonance features. The excitonic peaks of BL-WS_2 (blue line) undergo a redshift compared to the single-layer case, with values of 1.996 ± 0.008 eV, 2.372 ± 0.008 eV, and 2.757 ± 0.003 eV for A, B, and C excitons, respectively.

In line with our recent investigation [44], the 3R stacked homobilayer shows a relative shift of the A exciton with respect to the single layer of approximately 26 meV. This trend is also confirmed by PL results shown in figure 1(d). A slight intensity drop can also be observed. Variations in the dielectric function of WS_2, which depend on the number of layers, can be explained by considering the effects of quantum confinement in the band structure [82].

In general, the dielectric properties of the environment, which surrounds mono- and few-layer TMDCs, can significantly influence their optical response [35, 82, 84]. In our case, the presence of hBN slightly affects both the energies and amplitudes of WS_2 excitons at room temperature, as can be observed by comparing the red and dashed black curves acquired for ML-WS_2, respectively with and without hBN encapsulation. Our findings are in line with the literature, where a small redshift of 20–30 meV is reported for the neutral exciton at low temperatures in the presence of hBN-capped WS_2 flakes compared to the uncapped ones [33]. The results shown in this work are complementary to the ones reported in [44] since they can be used as a reference when dealing with vdW heterostacks, where hBN is combined with TMDCs and other 2D materials.

In general, when dealing with vdW heterostructures it is fundamental to take into account that dielectric screening affects the electron–hole Coulomb interaction and results in a considerable modification of the quasiparticle bandgap and exciton binding energies, which both contribute to the shift of excitonic resonances. As a consequence, the use of hBN as encapsulating material is instrumental to control the local dielectric homogeneity and to fabricate high-quality vdW homo- and heterostructures [33, 35]. We believe that the deep knowledge of the optical properties (i.e. dielectric function and PL) of hBN-encapsulated vdW homo- and heterostacks by means of spectroscopies with a resolution at the micro- and nanoscale [85, 86] is pivotal for their exploitation in novel devices.

4. Conclusion

In this work, we reported the optical response of 'free' and hBN-encapsulated WS_2 on a SiO_2/Si substrate. The WS_2 flakes were grown via LqP-CVD process and sandwiched between two layers of hBN by using a semidry transfer approach. We studied a three-layer (hBN/ML-WS_2/hBN) and a four-layer (hBN/3R BL-WS_2/hBN) stack by means of ISE, PL and Raman spectroscopies. ISE enabled us to extract the complex dielectric functions across one single hBN-encapsulated WS_2 flake and locally evaluate the evolution of A, B, and C excitonic spectral features by passing from mono- to bilayer areas. In correspondence of 3R stacked homobilayer WS_2 a redshift of the exciton resonance energies was observed

(approximately 26 meV in correspondence of A exciton), together with a slight intensity drop, in line with recent results [44]. These findings were corroborated by PL spectra. In addition, by comparing the dielectric function of hBN-capped and uncapped WS_2, we found that hBN layers have a slight influence on the energies and amplitudes of WS_2 excitons at room temperature. The stiffening of the A_{1g} mode in the Raman spectra confirmed that the hBN intercalation between the WS_2 and the SiO_2/Si substrate can reduce the level of electron doping from SiO_2.

More in general, vertical stacks, in which hBN alternates with TMDC layers, have already proved interesting for engineering their own optical properties. We believe that thorough investigations of the local optical response of hBN-encapsulated 2D crystals with high optical quality by combining various optical techniques, such as ISE and PL, are required for the exploitation of the single 2D layers as building blocks of more complex and, possibly, technologically relevant, vdW homo- and heterostacks.

Data availability statement

All data that support the findings of this study are included within the article (and any supplementary files).

Acknowledgments

The research leading to these results has received funding from Compagnia di San Paolo (project STRATOS) and Ministero dell'Istruzione, dell'Università e della Ricerca: PRIN 2017 Grant No. 2017KFY7XF and Dipartimenti di Eccellenza 2018–2022. We acknowledge support from DAAD (German Academic Exchange Service) Research Grants—Short-Term Grants, 2021 (57552336) as well as by the DFG (ZA 146/43-1, Project No. 406041998, ZA 146/47-1). This research has also received funding from the European Union's Horizon 2020 research and innovation program under Grant Agreement No. 881603-GrapheneCore3.

ORCID iDs

Marzia Ferrera https://orcid.org/0000-0001-5611-9957
Apoorva Sharma https://orcid.org/0000-0002-2919-1862
Ilya Milekhin https://orcid.org/0000-0003-2018-6095
Yang Pan https://orcid.org/0000-0003-4902-8197
Domenica Convertino https://orcid.org/0000-0002-6115-9790
Simona Pace https://orcid.org/0000-0002-3947-0136
Giorgio Orlandini https://orcid.org/0000-0003-4494-2756
Ermes Peci https://orcid.org/0000-0001-8536-3705
Lorenzo Ramò https://orcid.org/0000-0001-7008-7226
Michele Magnozzi https://orcid.org/0000-0003-4512-8430
Camilla Coletti https://orcid.org/0000-0002-8134-7633
Georgeta Salvan https://orcid.org/0000-0002-2565-9675
Dietrich R T Zahn https://orcid.org/0000-0002-8455-4582
Maurizio Canepa https://orcid.org/0000-0002-5148-1233
Francesco Bisio https://orcid.org/0000-0003-1776-3023

References

[1] Novoselov K S, Jiang D, Schedin F, Booth T J, Khotkevich V V, Morozov S V and Geim A K 2005 *Proc. Natl Acad. Sci.* **102** 10451–3
[2] Geim A K and Grigorieva I V 2013 *Nature* **499** 419–25
[3] Splendiani A, Sun L, Zhang Y, Li T, Kim J, Chim C-Y, Galli G and Wang F 2010 *Nano Lett.* **10** 1271–5
[4] Mak K F, Lee C, Hone J and Heinz T F 2010 *Phys. Rev. Lett.* **105** 136805
[5] Chhowalla M, Shin H S, Eda G, Li L-J, Loh P and Zhang H 2013 *Nat. Chem.* **5** 263–75
[6] Manzeli S, Ovchinnikov D, Pasquier D, Yazyev O V and Kis A 2017 *Nat. Rev. Mater.* **2** 71033
[7] Ramasubramaniam A 2012 *Phys. Rev.* B **115** 115409
[8] Qiu D Y, da Jornada F H and Louie S G 2013 *Phys. Rev. Lett.* **111** 216805
[9] He K, Kumar N, Zhao L, Mak K F, Zhao H and Shan J 2014 *Phys. Rev. Lett.* **113** 02614
[10] Ugeda M M *et al* 2014 *Nat. Mater.* **13** 1091–5
[11] Yu H, Cui X, Xu X and Yao W 2015 *Natl Sci. Rev.* **2** 57–70
[12] Raja A *et al* 2017 *Nat. Commun.* **8** 15251
[13] Mueller T and Malic E 2018 *npj 2D Mater. Appl.* **2** 29
[14] Chernikov A, Berkelbach T C, Hill H M, Rigosi A, Li Y, Aslan O B, Reichman D R, Hybertsen M S and Heinz T F 2014 *Phys. Rev. Lett.* **113** 076802
[15] Wang G, Chernikov A, Glazov M M, Heinz T F, Marie X, Amand T and Urbaszek B 2018 *Rev. Mod. Phys.* **90** 021001
[16] Eda G and Maier S A 2013 *ACS Nano* **7** 5660–5
[17] Kang K, Lee K-H, Han Y, Gao H, Xie S, Muller D A and Park J 2017 *Nature* **550** 229–33
[18] Zhong Y *et al* 2019 *Science* **366** 1379–84
[19] Kumar P *et al* 2022 *Nat. Nanotechnol.* **17** 182–9
[20] Jariwala D, Marks T J and Hersam M C 2017 *Nat. Mater.* **16** 170–81
[21] Song L, Song M, Lu Z, Yu G, Liang Z, Hou W, Liao Q and Song Y 2022 *Coatings* **12** 1152
[22] Gerber I C *et al* 2019 *Phys. Rev.* B **99** 035443
[23] Paradisanos I *et al* 2020 *Nat. Commun.* **11** 2391
[24] Peimyoo N *et al* 2021 *Nat. Nanotechnol.* **16** 888–93
[25] Zhang J, Hong H, Lian C, Ma W, Xu X, Zhou X, Fu H, Liu K and Meng S 2017 *Adv. Sci.* **4** 1700086
[26] Yu H, Liu G-B, Tang J T, Xu X and Yao W 2017 *Sci. Adv.* **3** e1701696
[27] Jin C *et al* 2019 *Nature* **567** 76–80
[28] Jin C *et al* 2019 *Nat. Phys.* **15** 1140–4
[29] Singh J and Soni R K 2020 *New J. Chem.* **44** 14936–46
[30] Singh J and Soni R K 2021 *Sci. Rep.* **11** 15352
[31] Singh J, Rishikesh, Kumar S and Soni R K 2020 *J. Alloys Compd.* **849** 156502
[32] Song L *et al* 2010 *Nano Lett.* **10** 3209–15
[33] Cadiz F *et al* 2017 *Phys. Rev.* X **7** 021026
[34] Pace S, Martini L, Convertino D, Keum D H, Forti S, Pezzini S, Fabbri F, Mišeikis V and Coletti C 2021 *ACS Nano* **15** 4213–25
[35] Raja A *et al* 2019 *Nat. Nanotechnol.* **14** 832–7
[36] Genco A, Trovatello C, Louca C, Watanabe K, Taniguchi T, Tartakovskii A I, Cerullo G and Dal Conte S 2022 *Phys. Status Solidi* b 2200376
[37] Qian C, Villafañe V, Soubelet P, Hötger A, Taniguchi T, Watanabe K, Wilson N P, Stier A V, Holleitner A W and Finley J J 2022 *Phys. Rev. Lett.* **128** 237403

[38] Stanev T K, Liu P, Zeng H, Lenferink E J, Murthy A A, Speiser N, Watanabe K, Taniguchi T, Dravid V P and Stern N P 2022 *ACS Appl. Mater. Interfaces* **14** 23775–84
[39] Woods C R, Ares P, Nevison-Andrews H, Holwill M J, Fabregas R, Guinea F, Geim A K, Novoselov K S, Walet N R and Fumagalli L 2021 *Nat. Commun.* **12** 347
[40] Vizner Stern M, Waschitz Y, Cao W, Nevo I, Watanabe K, Taniguchi T, Sela E, Urbakh M, Hod O and Ben Shalom M 2021 *Science* **372** 1462–6
[41] Yasuda K, Wang X, Watanabe K, Taniguchi T and Jarillo-Herrero P 2021 *Science* **372** 1468–72
[42] Wang X, Yasuda K, Zhang Y, Liu S, Watanabe K, Taniguchi T, Hone J, Fu L and Jarillo-Herrero P 2022 *Nat. Nanotechnol.* **17** 367–71
[43] Magnozzi M *et al* 2021 *J. Phys. Chem.* C **125** 16059–65
[44] Peci E *et al* 2023 *Adv. Mater. Interfaces* **10** 2201586
[45] Jung I, Vaupel M, Pelton M, Piner R, Dikin D A, Stankovich S, An J and Ruoff R S 2008 *J. Phys. Chem.* C **112** 8499–506
[46] Wurstbauer U, Röling C, Wurstbauer U, Wegscheider W, Vaupel M, Thiesen P H and Weiss D 2010 *Appl. Phys. Lett.* **97** 231901
[47] Albrektsen O, Eriksen R L, Novikov S M, Schal D, Karl M, Bozhevolnyi S I and Simonsen A C 2012 *J. Appl. Phys.* **111** 064105
[48] Funke S, Miller B, Parzinger E, Thiesen P, Holleitner A W and Wurstbauer U 2016 *J. Phys.: Condens. Matter* **28** 385301
[49] Sigger F, Lambers H, Nisi K, Klein J, Saigal N, Holleitner A W and Wurstbauer U 2022 *Appl. Phys. Lett.* **121** 071102
[50] Kim H *et al* 2017 *Nanotechnology* **28** 36LT01
[51] Conti S *et al* 2020 *Nat. Commun.* **11** 3566
[52] Ferrera M *et al* 2022 *Chemosensors* **10** 120
[53] Pace S *et al* 2021 *J. Phys. Mater* **4** 024002
[54] Chubarov M *et al* 2021 *ACS Nano* **15** 2532–41
[55] Forti S *et al* 2017 *Nanoscale* **9** 16412–9
[56] Mišeikis V *et al* 2015 *2D Mater.* **2** 014006
[57] Mišeikis V, Bianco F, David J, Gemmi M, Pellegrini V, Romagnoli M and Coletti C 2017 *2D Mater.* **4** 021004
[58] Coletti C, Giambra M, Mišeikis V and Romagnoli M 2020 WO/2020/201876 (available at: https://patentscope.wipo.int/search/en/detail.jsf?docId=WO2020201876)
[59] Kim K K *et al* 2012 *Nano Lett.* **12** 161–6
[60] Kim K K, Hsu A, Jia X, Kim S M, Shi Y, Dresselhaus M, Palacios T and Kong J 2012 *ACS Nano* **6** 8583–90
[61] Fujiwara H 2007 *Spectroscopic Ellipsometry: Principles and Applications* (Chichester: Wiley)
[62] Xia M, Li B, Yin K, Capellini G, Niu G, Gong Y, Zhou W, Ajayan P M and Xie Y-H 2015 *ACS Nano* **9** 12246–54
[63] Blake P, Hill E W, Castro Neto A H, Novoselov K S, Jiang D, Yang R, Booth T J and Geim A K 2007 *Appl. Phys. Lett.* **91** 063124
[64] Berkdemir A *et al* 2013 *Sci. Rep.* **3** 1755
[65] Zheng S, Sun L, Zhou X, Liu F, Liu Z, Shen Z and Fan H J 2015 *Adv. Opt. Mater.* **3** 1600–5
[66] Zeng H *et al* 2013 *Sci. Rep.* **3** 1608
[67] Debnath A, Kumar Shaw B, Bhattacharya S and Saha S K 2020 *J. Phys. D: Appl. Phys.* **53** 225004
[68] Chakraborty B, Bera A, Muthu D V S, Bhowmick S, Waghmare U V and Sood A K 2012 *Phys. Rev.* B **85** 161403(R)
[69] Buscema M, Steele G A, van der Zant H S J and Castellanos-Gomez A 2014 *Nano Res.* **7** 561–71
[70] Han X, Lin J, Liu J, Wang N and Pan D 2019 *J. Phys. Chem.* C **123** 14797–802
[71] Guide to Using WVASE Spectroscopi Ellipsometer Data Acquisition and Analysis Software 2012 (Lincoln, NE: J.A. Woollam)
[72] Artús L, Feneberg M, Attaccalite C, Edgar J H, Li J, Goldhahn R and Cuscó R 2021 *Adv. Photonics Res.* **2** 2000101
[73] Cappellini G, Satta G, Palummo M and Onida G 2011 *Phys. Rev.* B **64** 035104
[74] Segura A, Artús L, Cuscó R, Taniguchi T, Cassabois G and Gil B 2018 *Phys. Rev. Mater.* **2** 024001
[75] Lee S-Y, Jeong T-Y, Jung S and Yee K-J 2019 *Phys. Status Solidi* B **256** 1800417
[76] Wilson J A and Yoffe A 1969 *Adv. Phys.* **18** 193
[77] Jellison G Jr and Modine F 1996 *Appl. Phys. Lett.* **69** 371
[78] Herzinger C M and Johs B D 1998 US5796983 (available at: https://patentimages.storage.googleapis.com/12/ee/16/f6923133e8c0f6/US5796983.pdf)
[79] Johs B, Herzinger C, Dinan J, Cornfeld A and Benson J 1998 *Thin Solid Films* **313** 137–42
[80] Magnozzi M, Ferrera M, Piccinini G, Pace S, Forti S, Fabbri F, Coletti C, Bisio F and Canepa M 2020 *2D Mater.* **7** 025024
[81] Ermolaev G A *et al* 2021 *Nat. Commun.* **12** 854
[82] Li Y, Chernikov A, Zhang X, Rigosi A, Hill H M, van der Zande A M, Chenet D A, Shih E-M, Hone J and Heinz T F 2014 *Phys. Rev.* B **90** 205422
[83] Kozawa D *et al* 2014 *Nat. Commun.* **5** 4543
[84] Kajino Y, Oto K and Yamada Y 2019 *J. Phys. Chem.* C **123** 14097–102
[85] Ferrera M, Rahaman M, Sanders S, Pan Y, Milekhin I, Gemming S, Alabastri A, Bisio F, Canepa M and Zahn D R T 2022 *Appl. Phys. Rev.* **9** 031402
[86] Pan Y *et al* 2022 *Nanoscale Adv.* **4** 5102–8